

International Conference on Space Optics—ICSO 2022

Dubrovnik, Croatia

3–7 October 2022

Edited by Kyriaki Minoglou, Nikos Karafolas, and Bruno Cugny,



ALADIN UV LIDAR Instrument beyond 3 years in Space



ALADIN UV LIDAR Instrument beyond 3 years in Space

Paolo Bravetti ^a, Géraud de Villele ^a, Mickaël Olivier^a, Sylvain Arnaud^a, Marc Schillinger^a, Olivier Lecrenier ^a, Bertrand Corselle ^a, Didier Bon ^a, Sophie Jallade ^a

^aAirbus Defence and Space

ABSTRACT

AEOLUS underwent a long development led by Airbus Defence and Space both for the LIDAR instrument (ALADIN) in France, and the platform in the UK, and was successfully launched into a Sun-synchronous 320 km dawn-dusk orbit by a Vega launcher in August 2018.

The ALADIN Doppler wind LIDAR is pioneering the application of such kind of instrument in space and widens the field for space based LIDAR applications. Initially the mission was designed to be a demonstrator but can be actually considered as operational as the data are used routinely with positive impact on the Numerical Weather Predictions (NWP) models after less than one year of operations in-orbit.

After four years of operational lifetime, and also thanks to a strong support to in-flight operations, AIRBUS has learnt, together with ESA customer and scientist user teams, many things about ALADIN LIDAR instrument behavior and its performance monitoring in orbit.

While temperature and power telemetries monitoring are quite standard in post-delivery, the follow up of the instrument optical alignment and performance is less direct and lesson learnt show it can be however very profitable in particular for the first UV LIDAR in orbit.

The ALADIN architecture is recalled with its measurement principle, and its calibration mode and measurement mode, summarizing the available data for monitoring its behavior in orbit: this covers far field pattern from the atmospheric echo, or near field pattern from the atmospheric echo or internal calibration path; this allows to derive alignment stability of the transmitter and receiver part of the instrument. Also, spectral calibration curves trends allow to retrieve information's about spectrometers stability. In addition, energy monitoring trend are presented with several means available, and linked lessons learnt are driven.

As an important contributor for ALADIN performances, the telescope stability is analyzed and thermal correlation presented with representative Earth albedo maps. The telescope stability is shown as a contributor to link budget but also to spectrometers systematic error limitation due to their sensitivity to variations of divergence and line of sight (angle of incidence).

As other key element, the CCD sensor "hot pixel" observation is described with the workaround solution operation at instrument allowing to remove their negative impact on measurement data.

Overall conclusion is driven with lessons learnt and perspective for a follow on instrument.

Keywords: Aeolus, ALADIN, UV, Doppler wind LIDAR, remote sensing,

1. INTRODUCTION

AEOLUS is a European Space Agency Earth Explorer Core Mission. The primary objective of the mission is to provide wind measurements on a vertical atmospheric range over a global scale, with feeding numerical weather prediction (NWP) models. The mission was meant as demonstrator of wind Doppler LIDAR instrument. As a matter of fact ALADIN sole payload of the AEOLUS satellite is the first UV Doppler wind LIDAR in space and is the only UV LIDAR still operating in orbit since more than 4 years.

Airbus Defence and Space has been prime for the satellite mission and prime for the LIDAR instrument.

The ALADIN LIDAR development has been more complex than expected, mainly due to the handling of the UV laser source and the related challenges: power efficiency and dissipation, stability, reliability, emission path sensitive optics contamination and damage.

The first wind measurements were recorded less than 3 weeks after the launch that took place on August 22nd 2018, [1]. Following a commissioning phase of few months till the end of 2018 the satellite entered to its phase E2 where the data were delivered on regular manner; it could be seen in the course of the few months after launch the positive impact of the data on weather prediction. In fact since January 2020, starting with ECMWF (European Center for Medium-Range Weather Forecast) 0 most of European meteorology institutions did start to include AEOLUS data into the NWP on an operational basis.

This has been the results of extraordinary efforts spent over many long years of the ALADIN instrument development together with excellent work with users on the in orbit data analysis.

The Airbus instrument team has been involved on the in-orbit operations setting and data analysis supporting ESA and the DISC team (Data, Innovation and Science Cluster).

The present paper illustrate some of the instrument calibration modes and the relevant monitoring results and their implication in LIDAR data quality. It covers ALADIN operational period starting from the switch to laser B in June 2019 and started to be fully operative at the beginning of July 2019.

2. ALADIN ARCHITECTURE AND MONITORING FOR FLIGHT

The following figure recalls the optical architecture of ALADIN instrument. The laser heads generated UV beam is emitted through the large telescope of 1.5m diameter; an internal reference beam is sampling the laser beam and is redirected toward internal spectrometer after attenuation.

The atmospheric echo is collected back through the telescope and filtered spectrally and spatially before entering to the spectrometers section MSP (Mie Spectrometer) and RSP (Rayleigh spectrometer). In this spectrometers section the atmospheric echo Doppler frequency shift is recorded with two different approach corresponding to the most suitable design for Mie and Rayleigh backscattered signal.

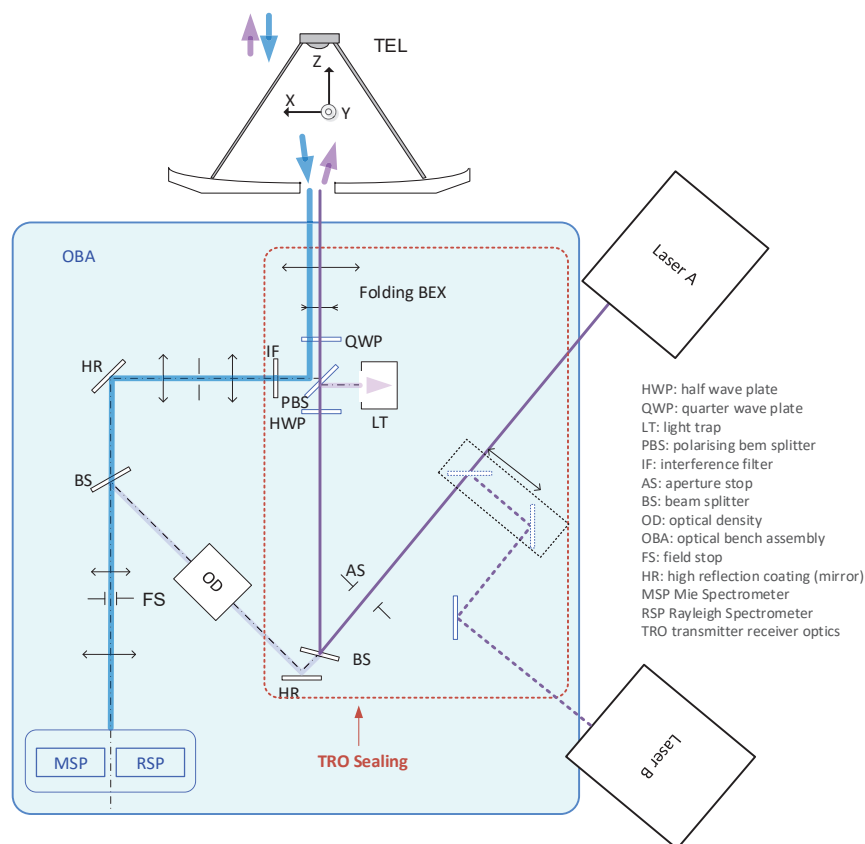


Figure 2-1 simplified optical sketch of ALADIN instrument

The next figure shows a close up view on the spectrometers section: the MSP is a Fizeau interferometer that produces a fringe which position is recorded on a detector to determine corresponding frequency shift. The RSP is a double Fabry Perot Etalon used in the double edge detection technique of the Rayleigh spectrum. The two etalon signals 1 and 2 are recorded on a dedicated sensor. Those signal ratios are used to derive the Rayleigh spectrum Doppler shift.

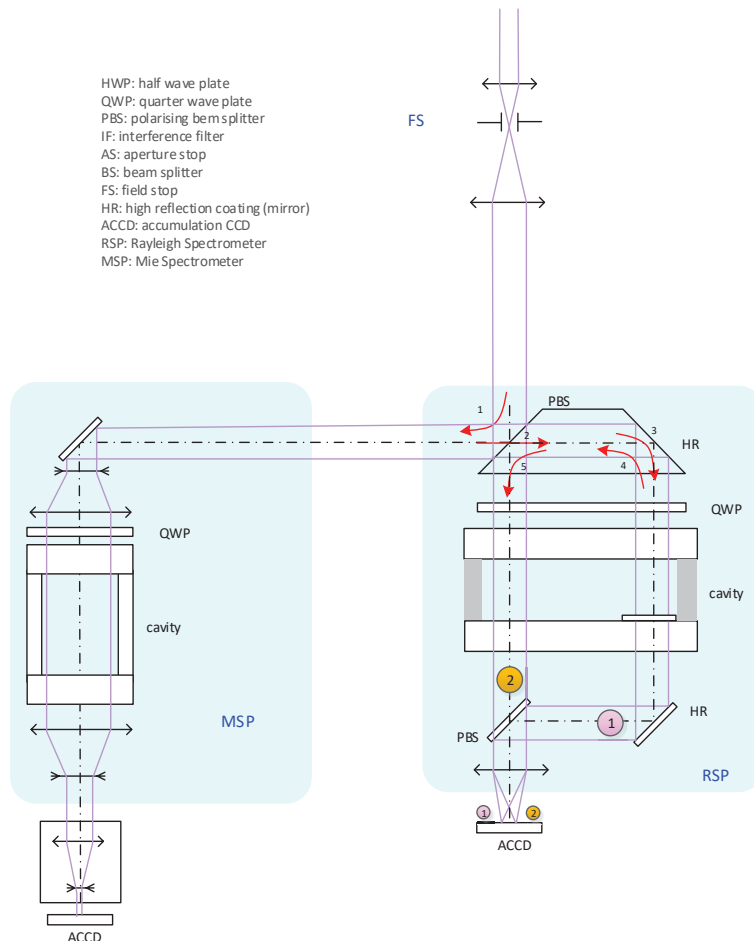


Figure 2-2 close up on Mie and Rayleigh spectrometer optical assembly after Field Stop

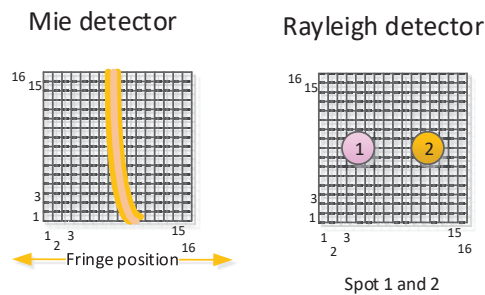


Figure 2-3 Mie and Rayleigh spectrometer detector

The sensors of the spectrometers can be used to monitor instrument internal properties independently from data science results or even pure calibration objectives.

As can be noticed in Figure 2-2 the MSP detector is placed after an afocal optic which allows to have an overview on the near field beam and also the pupil illumination. The RSP detector is at focal point, which provide information about the divergence value but behind the field stop and beam incidence angle.

During the AEOLUS mission time, routine performance and calibration measurements are performed. The analysis of the data acquired is used to derive some key instrument performance parameters and monitor its good health. The following list reports the calibration mode presented in this document:

- **LBM** – Laser Beam Monitoring: the emit beam is imaged on the Mie and Rayleigh detectors (near and far field respectively) via the Internal Calibration path, to derive spot centroid and size evolution with time
- **IDC** – Instrument Defocus Characterization: the received laser beam from the Atmospheric path is acquired by the Rayleigh detector to compute the spot centroid and size evolution with time
- **MRC** – Mie channel Response Calibration: response intensity is gathered while sweeping the emit frequency during Instrument Response Calibration (IRC, characterization of the receiver in nadir pointing, zero-wind conditions) to calculate the slope and intercept of the signal intensity vs. frequency, for both atmospheric path (and ground echo) and internal reference path
- **RRC** – Rayleigh channel Response Calibration: as for MRC, slope and intercept for both atmospheric path (ground echo and atmospheric echo) and internal reference path from the Rayleigh detector
- **ISR** – Instrument Spectral Calibration: acquisition of both spectrometer response signals from the internal optical path while sweeping the emit frequency. The data are evaluated in terms of Rayleigh channel spectral transfer function (peak central wavelength and Finesse)

These calibration are performed on a weekly basis. Some of them are also performed during special activities such as instrument set point tuning, to measure the effect of the different control parameters.

The acquisition of the beam spot properties, both from the internal calibration path or the atmospheric return, is done thanks to the two instrument detectors on the Mie and the Rayleigh spectrometers. Those detectors are 16x16 pixel matrix.

In addition, we report the evolution of the following quantities:

- Radiometric signals collected through both internal reference path and atmospheric path by the Rayleigh detector,
- Number of Hot Pixels i.e. pixels with higher dark current that need to be corrected.

The field stop corresponds to a FoV of 18.1 μ rad at TEL output and to 3.75 pixels on the Rayleigh ACCD.

The centroid and size of a beam spot are usually computed, respectively, as the center of gravity and the second moment of the intensity distribution.

$$\bar{i} = \frac{\sum_{i_{min}}^{i_{max}} i \cdot y_i}{\sum_{i_{min}}^{i_{max}} y_i} \quad \sigma_i = \sqrt{\frac{\sum_{i_{min}}^{i_{max}} (i - \bar{i})^2 \cdot y_i}{\sum_{i_{min}}^{i_{max}} y_i}}$$

Where i is the column or row index:

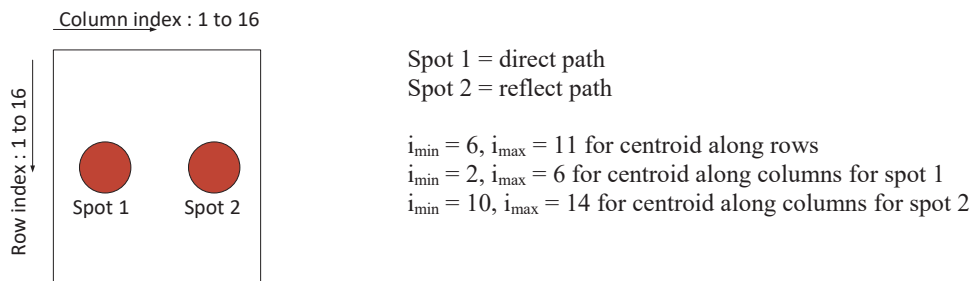


Figure 2-4: spot identification and index numbering on the Rayleigh detector matrix

To be robust to electrical noise, beam spots acquired with the nominal instrument processing were fitted with a 2D Gaussian function with 5 free parameters: amplitude, x and y positions and x and y widths. This method is used to derive the parameters reported in this document for both Rayleigh and Mie spots.

3. RESULTS

3.1 Laser Beam Monitoring

During the Laser Beam Monitoring (LBM) the laser frequency is varied by 1.5 GHz around its set point to cover the CCD equivalent spectral width, which is almost a Free Spectral Range (FSR) of the Mie spectrometer (about 2.2 GHz). At each frequency, a fringe image is transmitted by the Fizeau spectrometer. The laser beam spot is reconstructed through the superposition of the fringes acquired in this way during the sweeping. The resulting image represents the laser beam near field pattern and the position and size at different optical path levels can be computed.

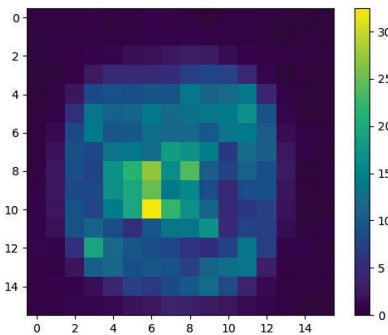


Figure 3-1 : Laser beam near field (INT ref path) after reconstruction through the LBM procedure.

On the Rayleigh detector, the frequency sweeping impacts the relative intensity of the two spots (direct and reflected) from the Fabry-Perot spectrometer. The average of the images acquired at the various frequencies is used for far field beam analysis, to compute the line of sight (incidence angle) and divergence variations, as seen after the filtering of the field stop.

Figure 3-2 shows the evolution of the Rayleigh spot centroid position and radius, resulting from Gaussian beam fitting over the analysed period and over the entire laser B operation period. Figure 3-3 reports the beam centroid position displacement in X-Y plot. The units of the following plots are in pixel. The “col” direction is horizontal at the CCD, the “row” one is vertical.

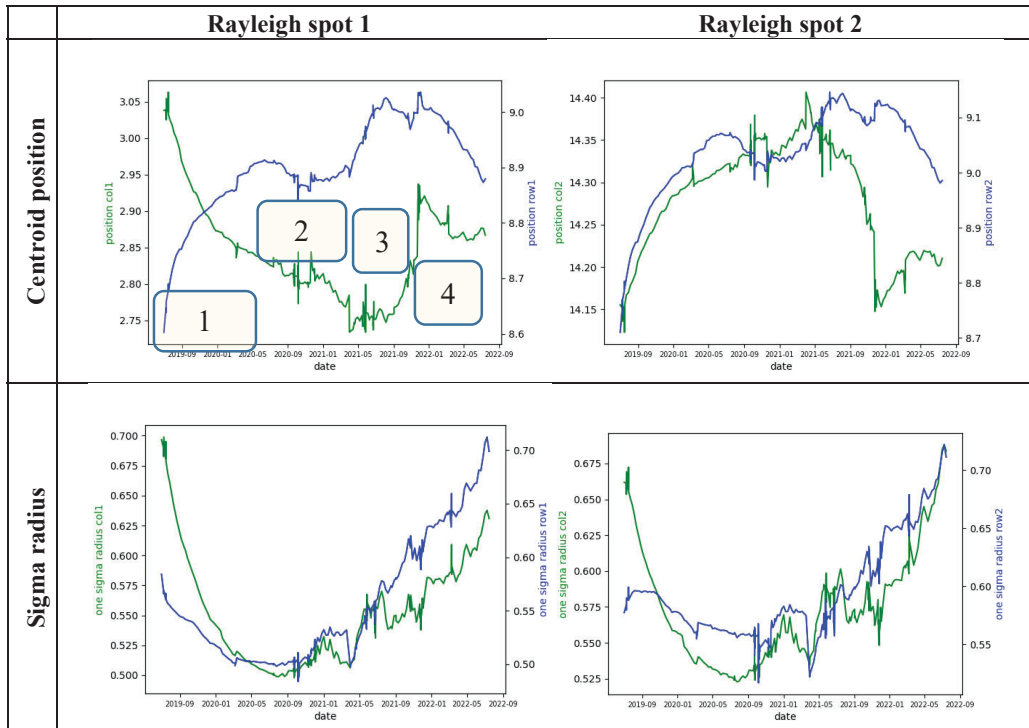


Figure 3-2: LBM Rayleigh spot centroid position and radius evolution resulting from Gaussian beam, over the analysed period and over the entire laser B operation period.

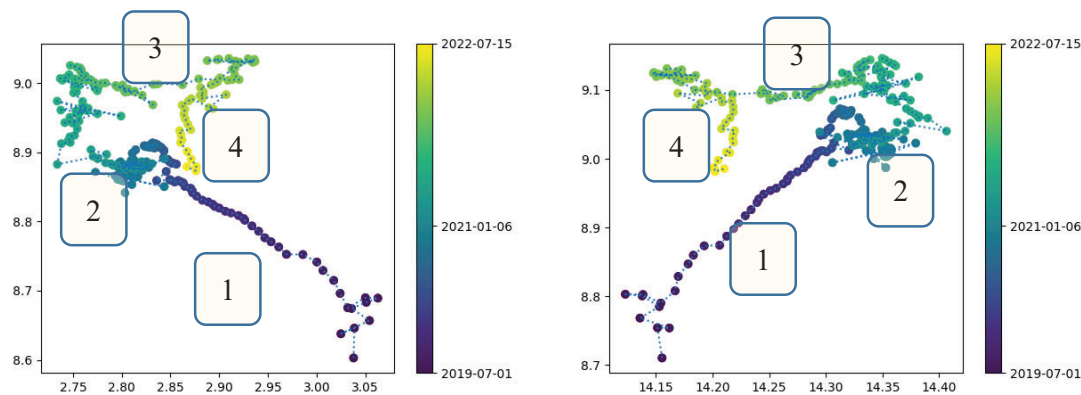


Figure 3-3: INT Ref Rayleigh spot 1 (left) and spot 2 (right) position from Gaussian fit of L1B data images over the entire laser B operations; colors correspond to time.

The vertical drift is lower in the central period (regions “2” and “3”) and moves backward in the last period (region “4”). The horizontal position is similar to the vertical one in the first half of the period (regions “1” and “2”), while it strongly drifts in the opposite direction starting in the second half of 2021 (region “3”) which includes an unintentional instrument switch-off occurred in October 2021 and operations performed to intentionally move spot 1 to the right (the rapid variation between regions “3” and “4”). Then, it slightly moved back to the left and settled (region “4”): the last recorded position along columns is much closer to the one measured at the beginning of operations, although some evidence of spot clipping on the field stop [2] could impact the result of Gaussian fits.

The measurement noise is higher in the second half of the period (regions “2” and “3”) compared to first part (region “1”). This is probably due to the lower signal intensity detected on the internal reference optical path (see section 3.5) and the probable clipping. Additional noise is linked to operations on the instrument (variation of the set point), in particular to the mentioned switch-off events, which perturbed the instrument thermal conditions.

Figure 3-3 shows Gaussian fit centroid displacement in X-Y plots for the two spots: from the optical sketch of Figure 2-1 one would expect perfectly symmetric spots displacement between 1 and 2. However the plot evidences an asymmetry between the two Rayleigh spots, which is not fully understood: in particular a larger displacement on spot 2 is observed around mid-2021 (see region “3”). The displacement observed afterwards, including the one due to instrument restart and set point variation, is instead similar for the two spots.

The drift could be linked either to laser line of sight evolution or to the same root cause at the origin of the return signal degradation.

The spot size decreases in the first half of the period and increased in the second half, especially along rows: consequently, the size is very close to the one measured at the start of FMB operations, but with an inversion of aspect ratio. As there is probably a clipping of the spot, the real beam could be larger than the Gaussian fit results.

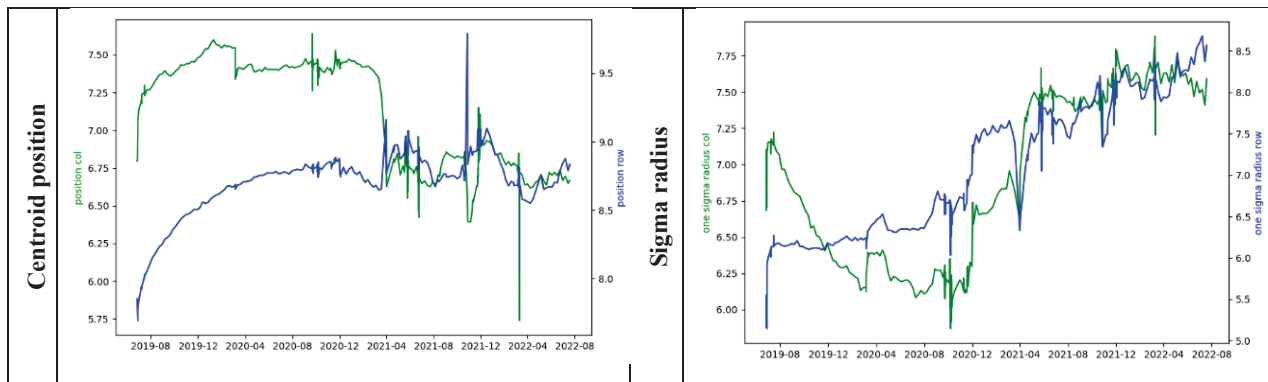


Figure 3-4: LBM Mie spot centroid position and radius evolution resulting from Gaussian beam fitting of raw instrument data (courtesy ESA), over the analyzed period and over the entire laser B operation period.

Figure 3-4 shows the evolution of the Mie spot position over the entire laser B operation period. As for the Rayleigh spots, the noise is larger in the second half of the period.

The centroid X and Y coordinates increase during the first months of operation. Then, they show some oscillations around the reached value (also linked to the in-flight operations). The horizontal position shows a drop in correspondence of the instrument switch off in March 2021. Now the spot centroid seems to be stable and oscillates around a position.

The beam size shows a strong increase probably due a change of beam energy distribution, with less smooth beam with few hot spots in the center as visible in Figure 3-6. This evolution is attributed to probable laser induced contamination (LIC) or laser induced damage (LID) on some optical surface in the internal optical path.

This LBM images evolution series are important clue to show long term beam evolution and need to be taken into account when trying to explain energy trends: laser induced damage or laser induced contamination are suspected.

The pixel fluence evolution is reported in blue in Figure 3-5. During the initial phase the pixel fluence increases despite the overall energy was decreasing. Fluence value then decreases in the same way as the radiometric signal (see section 3.5).

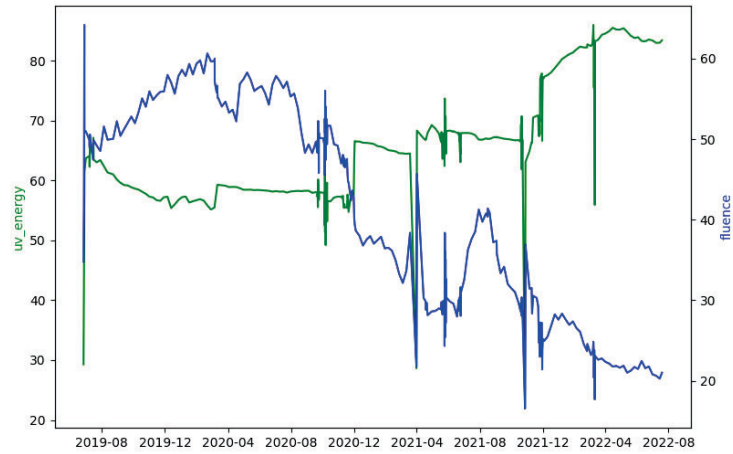
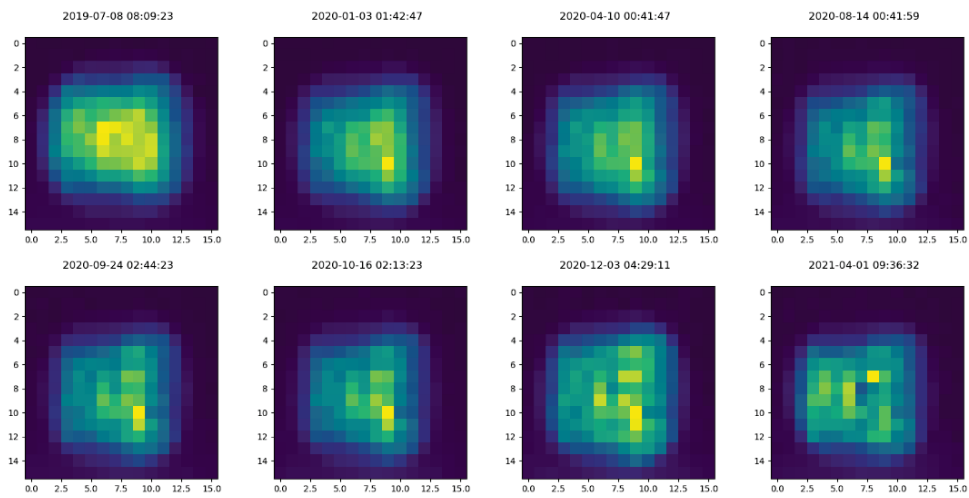


Figure 3-5: Evolution of laser energy and LBM Mie spot fluence, calculated from the Gaussian fit of raw instrument data (data courtesy ESA).



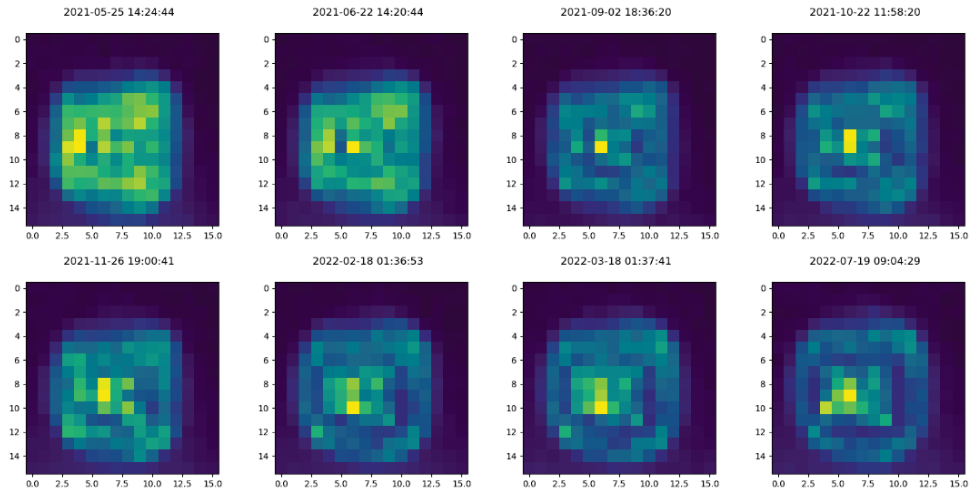


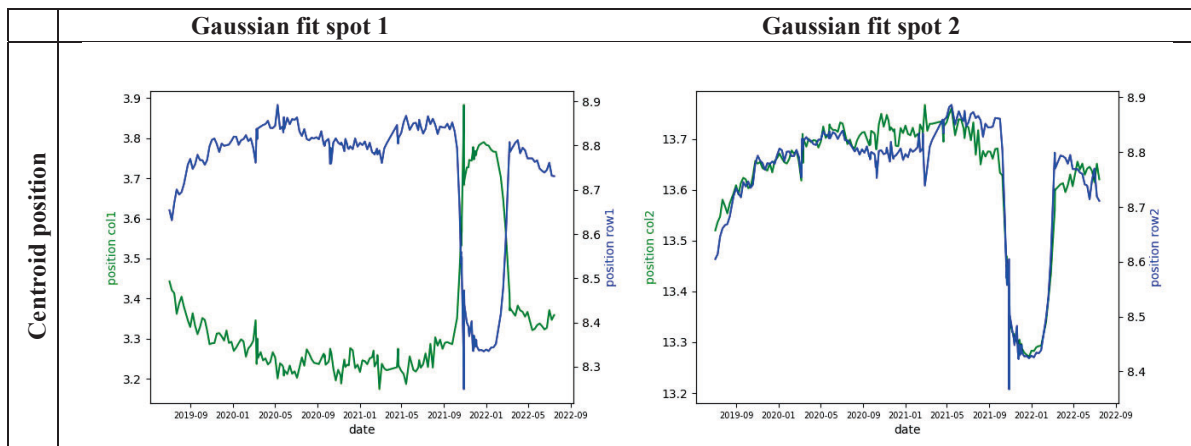
Figure 3-6: LBM Mie spots acquired during the entire operation time with min max color-bar

3.2 Instrument Defocus Check

The IDC (Instrument Defocus Check) acquires an image of the atmospheric return beam spot from the Rayleigh detector averaged over a few minutes in specific points along the orbital track.

The atmospheric path spots are representative of the received beam direction and divergence, i.e. they represent the far field of the received laser beam. As there is evidence that the spot is clipped at field stop level some care shall be taken in the interpretation of the spot centroid.

The following figures report the evolution of means centroid and mean one sigma radius of the Rayleigh spots acquired from the atmospheric optical path. The parameters are calculated with 2D Gaussian fit of the acquired images and the units are in pixel.



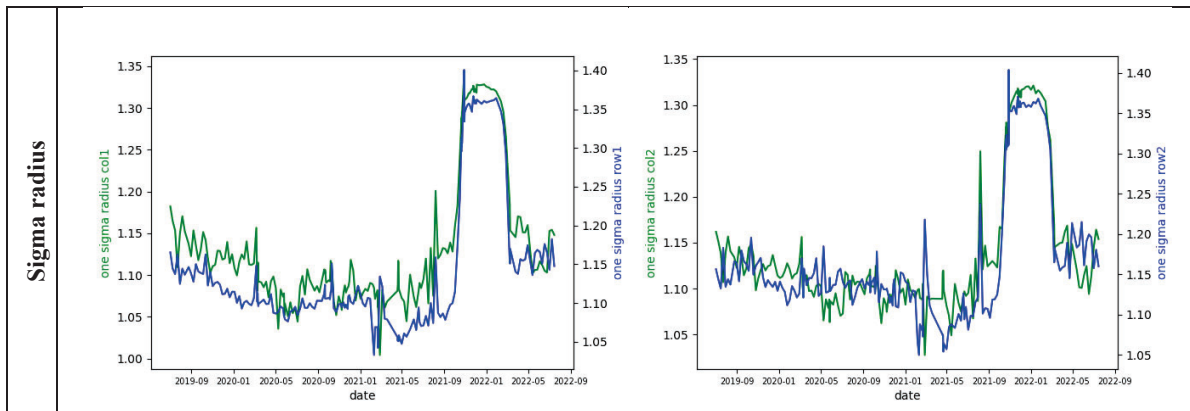


Figure 3-7: IDC centroid position and spot radius evolution resulting from Gaussian fit, over the analyzed period and over the entire laser B operation period.

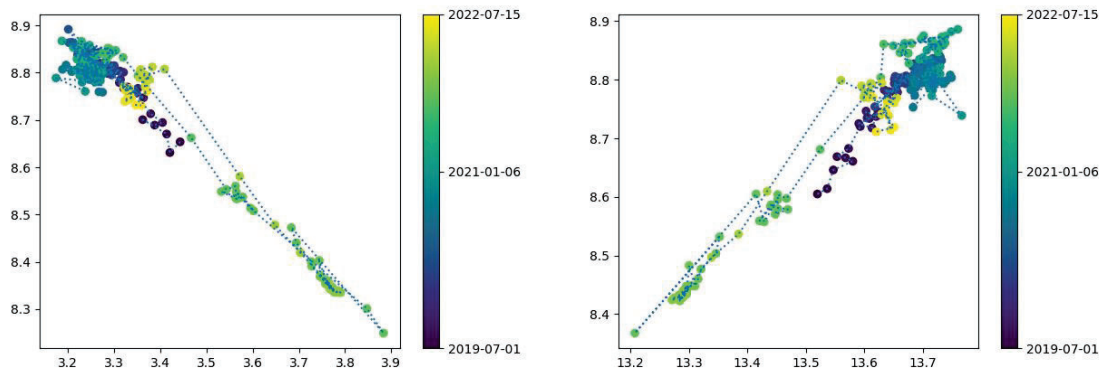


Figure 3-8: ATM path spot 1 (left) and spot 2 (right) centroid position in pixels from Gaussian fit, over the analyzed period (top) and over the entire laser B operations (bottom); colors correspond to time.

Figure 3-7 shows the evolution of IDC centroid position and spot radius evolution over the entire laser B operation period. Figure 3-8 shows an X-Y plot of the centroid displacement, which is diagonal during the last few months.

In the period between 15 October 2021 and 10 March 2022 a strong variation of all the IDC beam spot parameters is visible in the plots. This variation is clearly a seasonal effect and it is probably due to some stray-light illuminating the instrument field stop due to the variation of the sun tangent height during that period.

If we do not consider this variation, the spot position and size measured from IDC had an evolution similar to LBM spot: the centroid drift was stronger in the initial half of the period and settled in the second half; the size initially decreased and then slightly increased during the last period. Both position and size (with the exception of the period mentioned above) are rather stable through time, demonstrating a very good stability of the instrument.

3.3 Instrument Response Calibration

During the Instrument Response Calibration (IRC) the satellite is pointed to nadir and the response of the receiver in zero-wind conditions is characterized.

The emit frequency is linearly varied over about one free spectral range (FSR) of the Fabry-Perot Rayleigh spectrometer (11 GHz) and the responses of both spectrometers are acquired.

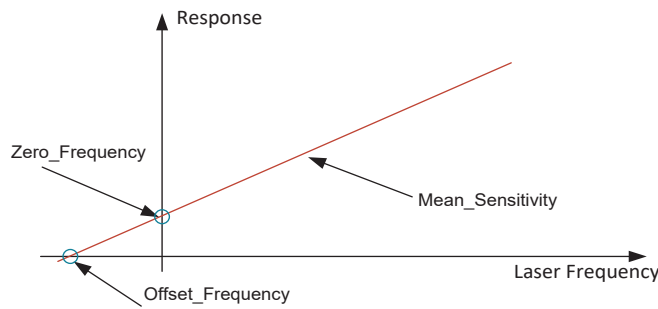


Figure 3-9 : main IRC response parameter definition

Figure 3-9 shows the slope (mean sensitivity) and intercepts (zero frequency and offset frequency) of the signal intensity vs. frequency, for both atmospheric path and internal reference path.

IRC measurements were performed before beginning of 2020 after mid-2021: in the intermediate period they were suspended while improving laser cooling system behavior during nadir maneuvers (found sometimes defective possibly triggering anomalies). Therefore in the following plots there is a period with no data available.

Before the IRC measurements were restarted, the laser frequency set point was changed to compensate a different reference laser locking mode (probably due to combination of thermal and ageing effects) at the instrument restart after an unintentional switch-off (beginning of 2021). As a result, the offset frequency (frequency for which the spectrometer response is zero) plots below have a discontinuity of about 1.5 GHz.

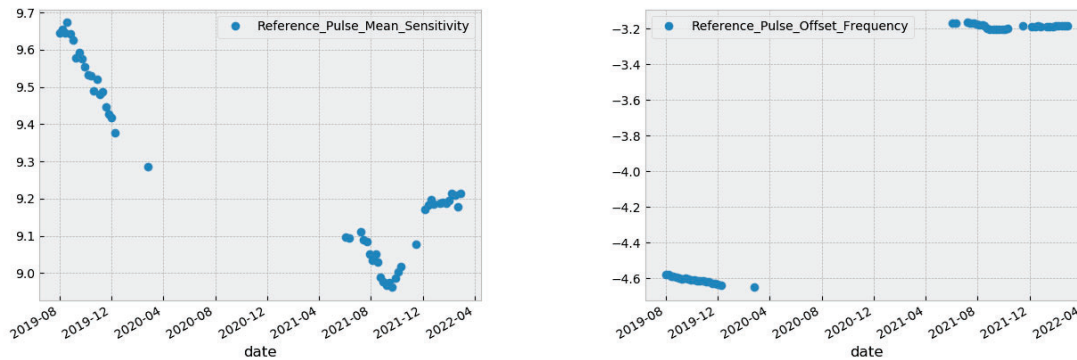


Figure 3-10: MSP – internal reference: slope on the left (MSP pixels/GHz) and offset frequency on the right (GHz)

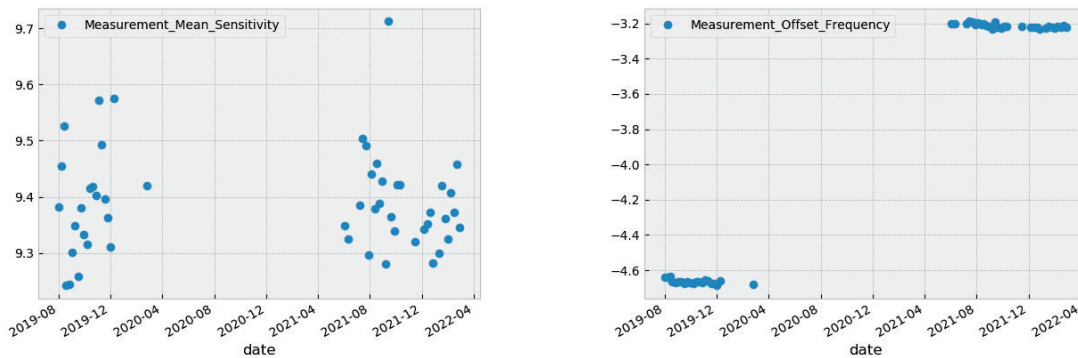


Figure 3-11: MSP – atmospheric path slope on the left (MSP pixels/GHz) and offset frequency on the right (GHz)

The visible part of the evolution of internal path sensitivity reported in Figure 3-10 has the same shape as the spot position reported in Figure 3-2: a variation along time of the transmitter line of sight could explain the observed evolution. Noise is dominating the atmospheric trends. Anyway, calibration parameters of both internal reference and atmospheric paths do not vary significantly through time showing a stable instrument behavior.

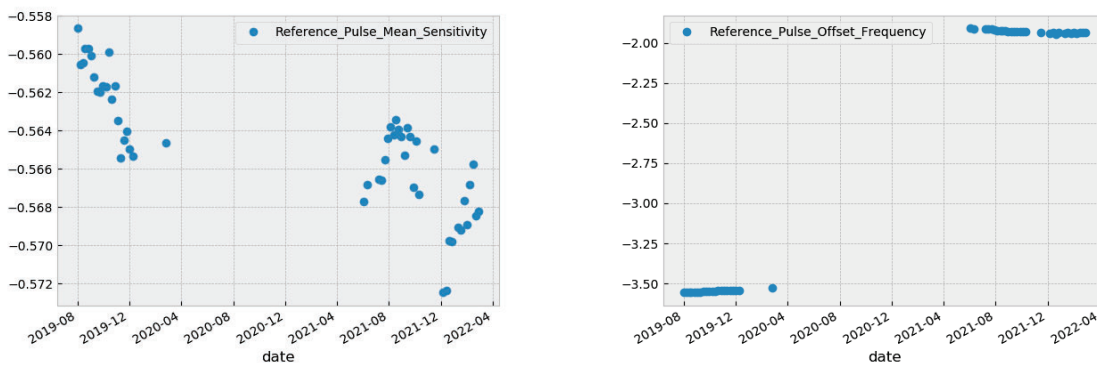


Figure 3-12: RRC – internal reference, slope on the left (1/GHz) and offset frequency on the right (GHz)

As for the MSP, also on RSP the internal reference slope there is some footprint of the beam LoS variation. RSP sensitivity and offset frequency for ground echo and atmospheric path are similar to MSP atmospheric path, with evident trend, and are thus not shown here.

The Rayleigh spectrometer calibration parameters are quite stable along the entire ALADIN operation time, with a sensitivity variation lower than 10%.

3.4 Instrument Spectral Registration

The ISR (Instrument Spectral Registration) consists in scanning the laser frequency over +/- 5.5 GHz and record the radiometric signal for each Rayleigh spot corresponding to the direct and reflect paths (see Figure 2-4). This is the spectral transfer function for each path.

A detailed study on the ISR data output has been presented by DLR team in [3][2], and details the calibration techniques and quantify several trends and drift from the data.

The laser energy, and therefore the transmit energy, depends on the frequency set point (due to laser oscillator design). Therefore the laser Rayleigh signal is corrected for the laser energy variation with respect to the frequency using the laser energy telemetry (PD74).

A regression analysis is carried out for each corrected spectral transfer function using the following models.

For the direct path

$$FPd(f, \vec{p}_d) = \frac{p_{d2}}{1 + 4 \cdot \frac{p_{d1}^2}{\pi^2} \sin^2\left(\frac{\pi[f - p_{d0}]}{FSR}\right)} + p_{d3}$$

For the reflect path

$$FPr(f, \vec{p}_r) = \left[1 - \frac{FPd(f, \vec{p}_d)}{FPd(f, \vec{p}_d)_{max}}\right] \cdot \frac{p_{r2}}{1 + 4 \cdot \frac{p_{r1}^2}{\pi^2} \sin^2\left(\frac{\pi[f - p_{r0}]}{FSR}\right)} + p_{r3}$$

being FSR the free spectral range and p_{d1}, p_{r1} : the effective finesse.

The direct path spectral transfer function model is fitted first in order to estimate the parameter set \vec{p}_d , then the reflect path transfer function is fitted using the reflect model.

The error function is the root mean squared.

$$RMSError(\vec{p}) = \sum_{i=1}^N \sqrt{\frac{(y_i - FP(f_i, \vec{p}))^2}{N}}$$

The spacing is defined as

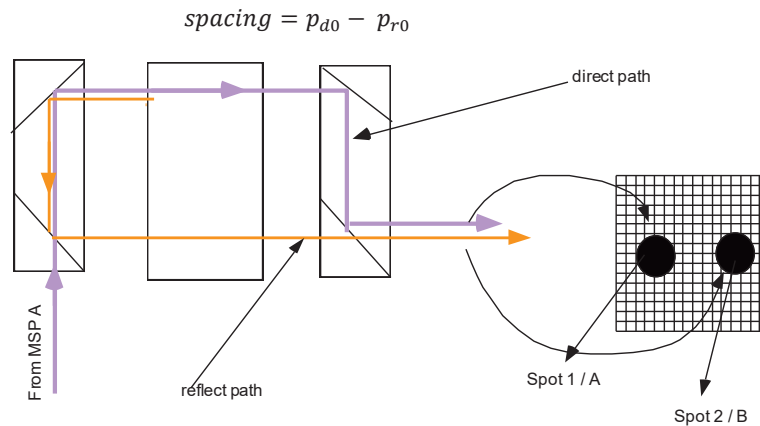


Figure 3-13: direct (spot 1=A) and reflect (spot2=B) path definition in Rayleigh spectrometer.

Figure 3-14 shows typical spectral transfer functions of the Rayleigh spectrometer (left) and the fit result with associated residuals for direct (center) and reflect (right) paths. It is possible to distinguish in the residual an oscillation corresponding to the Rayleigh channel input signal modulation by the Mie spectrometer which is placed first in the optical path. The period of the modulation is 2.2 GHz corresponding to the Mie spectrometer FSR.

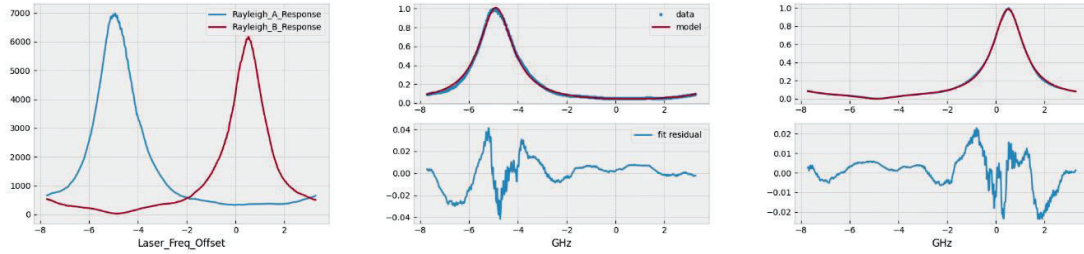


Figure 3-14: Rayleigh response (left), direct path (center) and reflect path (right) spectral transfer fit result and residuals of the last ISR performed in the analyzed period.

In general, the ISR measurement shows a very good repeatability. The following plots report the evolution of the main response parameters.

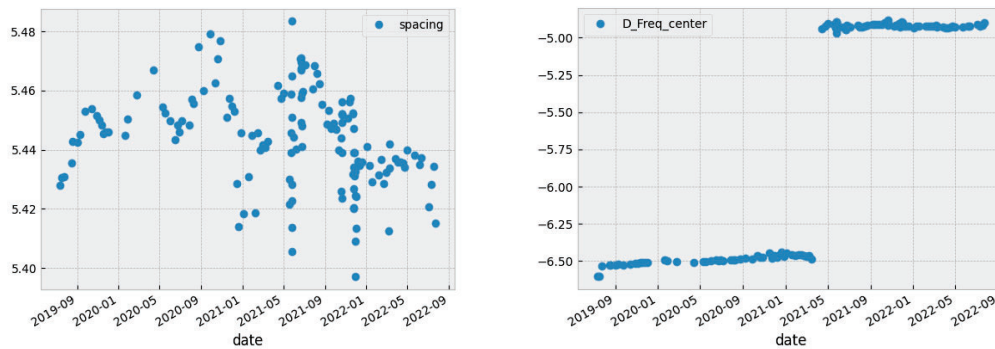


Figure 3-15: Evolution of direct-reflect peak spacing (left)(GHz) and direct central frequency (right)(GHz)

The Spacing from Figure 3-15 shows oscillations but it is overall stable over time (lower than 80 MHz). The slope of the center frequency is negligible (if we exclude the large discontinuity due to the different set points mentioned previously) confirming that there is no degradation of the spectrometer.

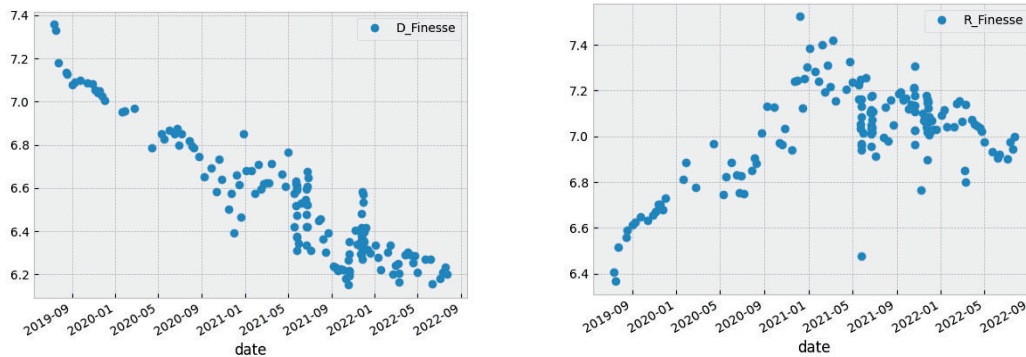


Figure 3-16: Evolution of direct path (left) and reflect path (right) finesse over time (no units)

The finesse slope over time reported in Figure 3-16 is about -0.03 /month for the direct path and about $+0.03$ /month for the reflect path, till beginning of 2021. The non-negligible linear evolution could be due to several causes: a laser LoS and divergence variation, a near field clipping or distortion (LIC/LID in the central region of the spot), a coating degradation or to a modelling artefact. The opposite sign variation of the two paths could be linked to symmetrical optical path considerations.

The trend of the finesse is still linear for the direct path, while it is saturated for the reflected path: the reflected path finesse is close to the theoretical reflectivity finesse (highest possible value) of this Fabry-Perot. Nonetheless, there are no evident limitations to instrument performance induced by this evolution.

3.5 Radiometric signal

Figure 3-17 shows the evolutions of the laser-B energy with time, the internal reference path Rayleigh signal and the atmospheric path Rayleigh signal. With the exception of the very first part of the time period, when also the laser signal is clearly decreasing, both internal and atmospheric signals are notably decreasing despite stable laser output energy (PD74).

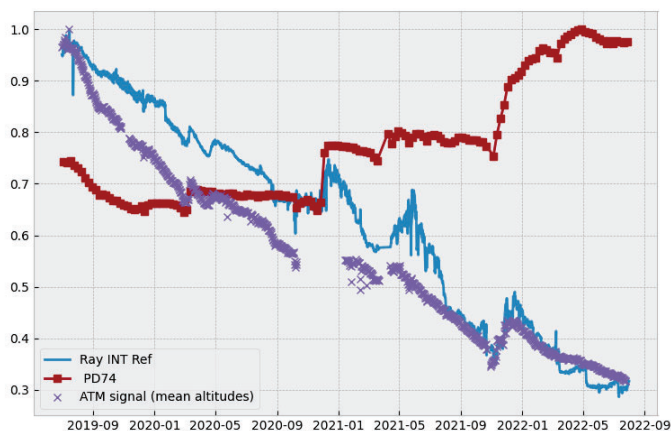


Figure 3-17: Comparison of the evolution of laser energy monitor photodiode (PD74), internal reference signal on the Rayleigh sensor (from lidar mode) and atmospheric Rayleigh return signal (mean of altitudes from 10 to 16km)

This observation could be attributed to LIC or LID on optical elements comprised between the laser output (after the monitoring photodiode) and the TRO (transmit-receive optics) diplexer, it could also be partly attributed to an increasing clipping effect at the small field stop size of $18\mu\text{rad}$; other root cause like a possible transmission loss due to irradiation could be possible. The strong degradation of the near field beam spot shape already shown in Figure 3-6 tends to confirm a LIC or LID contribution on optics path. So far, no single root cause could be confirmed definitely and quantitatively. The behavior on laser B displayed in above figure is however not common to laser A operations at mission start in 2018: during this laser A operation, the receiver energy was closely following the laser energy loss trend showing no additional loss on receiver optics side, in contradiction to laser B operations observation.

Further investigations are ongoing to discriminate root causes; end of life test for AEOLUS will be crucial opportunity to learn more, also with planned switch back on of the laser A.

3.6 Hot pixels

Some pixels from the storage area on both Mie and Rayleigh detector showed suddenly an increased dark signal level (output detector signal recorded when no optical radiation is present). They are called hot pixels.

These hot pixels when not corrected have an impact on the wind data errors; a detailed study has been presented in [4]. A calibration method allows to regularly and quickly calibrate the dark current without significant impact on LIDAR data collection operations.

The root cause of this dark signal increase has been studied by Airbus with support of T-e2v (detectors supplier) and several hypotheses have been elaborated and confirmed possible contributors. It has in particular been demonstrated that Clock Induced Charge (CIC) effect is involved in this anomaly, on the contrary to regular Hot Pixels, generated by displacement damage caused by energetic particles (mainly protons from the South Atlantic Anomaly for low Earth orbit satellites [2]). This can be connected to two specific ACCD features: its inverted operation in the storage area and the high amount of clocking applied to the device for its specific operation on ALADIN.

As one can observe from Figure 3-18, the number of hot pixels is linearly evolving during time since the beginning of the mission. In the last period a lower slope is observed for Rayleigh detector.

Indeed, an increase in solar activity has been recorded since last autumn due to the rise of the solar cycle. As AEOLUS is at 320km altitude, which is low compared to other satellites, it is thus more protected by the Earth's atmosphere against the intrusion of galactic ions. This could be a clue that galactic ions are involved in the root cause of this anomaly.

The position of the hot pixels in the ACCD storage area is reported in Figure 3-19 for both Mie and Rayleigh sensors.

While protons and galactic ions fluxes are expected to be anti-correlated with solar activity, electrons flux should increase with it.

In addition, due to its location inside the instrument/satellite the Rayleigh ACCD equivalent shielding is larger than the Mie ACCD one, and this could possibly explain the different evolution of hot pixels in the two detectors: for the Mie device, the decrease of protons rate is compensated by high energy electrons rate increase while the Rayleigh ACCD is better protected against electrons and is impacted mainly by the protons.

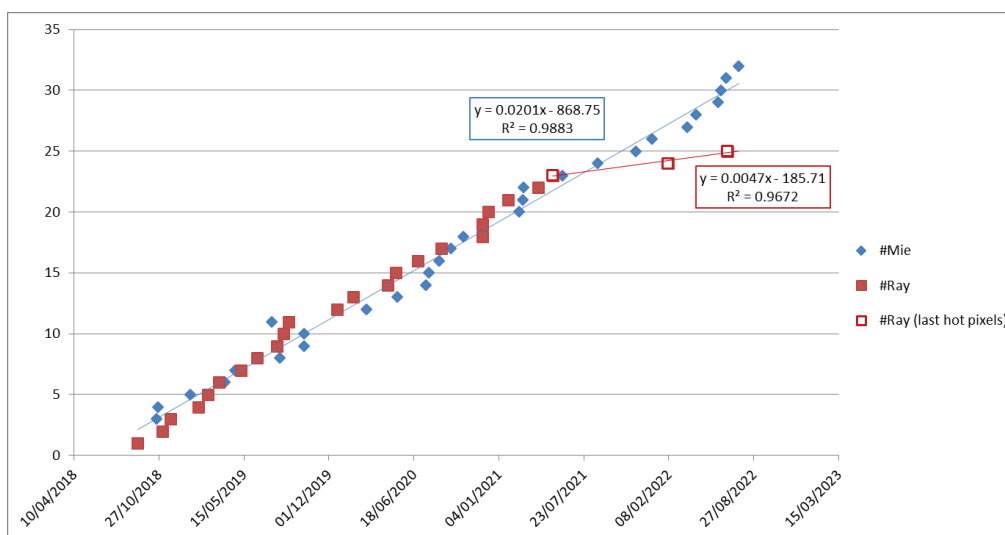


Figure 3-18: Evolution over time of Mie and Rayleigh detector hot pixels

Figure 3-20 reports the mapping of trapped electrons, trapped protons and the locations where any Hot Pixel has emerged. On the two first figures and as expected (even at the 320 km low altitude from Aeolus), the effect of the South Atlantic Anomaly (SAA) is visible in terms of protons and electrons. The reported particle fluxes are of the order of a few thousand / few tens of thousands per cm².s but after transporting them through a simplified version shields they go down to a few / few tens of particles per cm².s. This could explain why we see an SAA effect, but that it is not so marked.

Over the poles, the majority of particles are expected to be low LET ions (with high penetration capability) and high energy galactic protons. For both of them, the difference of Mie and Rayleigh shielding might not influence the HP statistics.

Outside SAA and poles, a preliminary analysis performed by Airbus considering any type of particles (trapped protons, trapped electrons, solar protons, cosmic ions and cosmic protons) is showing that particles with low flux (few per minute per cm²) can be expected everywhere over the Earth, flux being about 10 times lower than over SAA (considering Aeolus detectors shielding), and varying with latitude (except in SAA), the lower the latitude, the lower the flux.

As a conclusion, it cannot currently be excluded that all types of particles are contributing to the HP generation, in line with the observation of HP emergence outside SAA and poles.

This does not exclude that some could be due to the radiation generated of the detector window, which was also observed on ground.
It will be important to see how this mapping will evolve during the solar cycle, and if it will be possible to confirm and refine the trends depicted above.

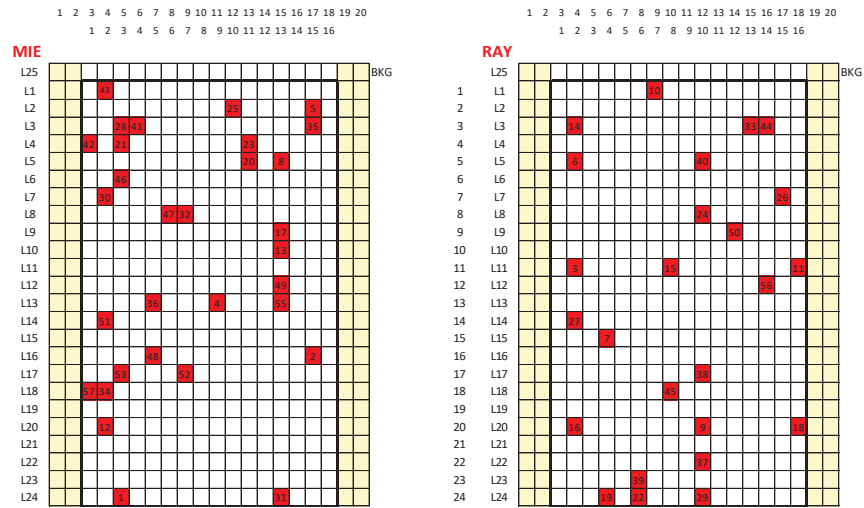
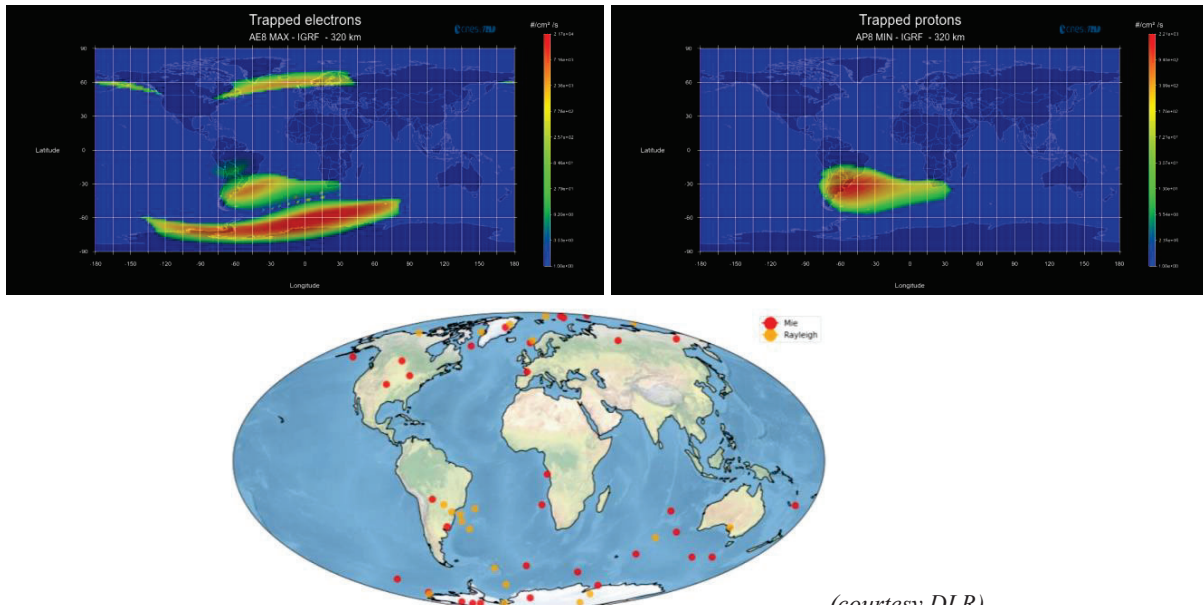


Figure 3-19: Hot pixel position with respect to the ACCD sensors storage area



(courtesy DLR)
Figure 3-20: Mapping of creation of hot pixels compared to mapping of radiation flux

4. TELESCOPE STABILITY AND LINK TO WIND SPEED BIAS

The in-flight temperature of the telescope secondary mirror (M2) and associated struts have a stability better than 10 mK over the orbit, the values are fully in line with the flight predictions (15 mK). But for the primary mirror (M1), it was observed that its stability was not as expected over the orbit while its mean temperature variation was well in line with predictions when going to Nadir calibration configuration.

When analyzing the wind speed bias data it was highlight a strong correlation to the M1 thermal gradient, this is shown in Figure 4-1 and presented in [5].

The M1 thermal gradient variations over the orbit induce M1 WFE variations and consequently modify slightly the shape of the instrument Point Spread Function (PSF) both in emission and reception as the instrument architecture is monostatic meaning that the Telescope is used in emission and reception. The PSF modification means a modification of the angular distribution at spectrometers input. As the spectrometer response is sensitive to angular variations, the M1 temperature variations translate in the end into an uncorrected wind speed bias.

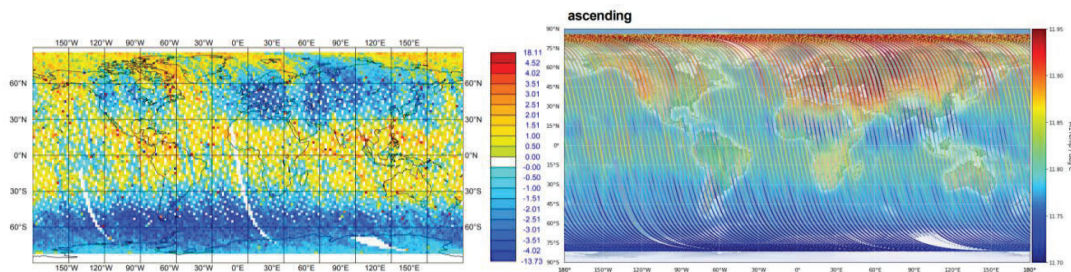
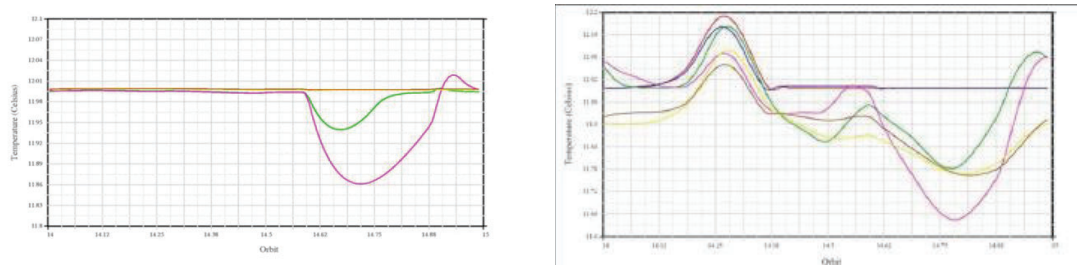


Figure 4-1 wind bias (left) and M1 average temperature (right) (courtesy M. Rennie, ECMWF).

In order to understand the link between the observed frequency bias and the M1 temperature variation, an investigation (STOP analysis) of the thermal and optical Telescope performances behavior has been triggered at Airbus in early 2020. Several major roots causes have been identified to explain and reproduce the inflight mirror M1 behavior.

In the frame of instrument design phase in the early 2000's, constant external fluxes (Earth albedo and IR) had been considered lacking more precise data. Since few years now, ESA external flux maps as a function of the latitudes and seasons can be used for more accurate simulations. Hence, the introduction of such maps have been added in the AEOLUS thermal model and the results have shown a real improvement in the inflight and model results comparison as per Figure 4-2.



Initial Model Flight comparison

Improved Model Flight comparison

Figure 4-2 Correlation improvement, Model/flight comparison

The green line on the top right chart of Figure 4-3 illustrates the total flux on mirror side (summer solstice). Evolution of M1 temperature is presented for illustration (correspondence to flux variation)

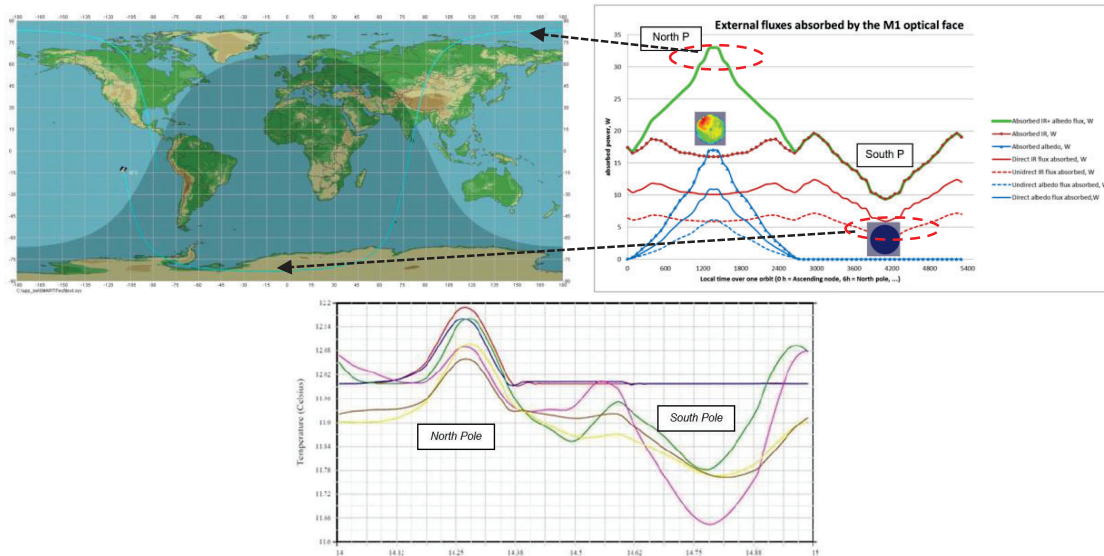


Figure 4-3 Flux over the orbit and M1 temperature evolutions

On the overall M1 surface, the extremes flux are the followings

- **North Pole:** Albedo power is higher than IR flux, total is absorbed is about 50.4 W
- **South Pole:** No more Albedo, IR flux is minimum during summer solstice, the absorbed flux is about 12.9 W

When looking in more details on the M1 absorbed power contributors in the analysis it can be observed that there is indirect thermal source from the telescope baffle reflection: this can contribute up to one third of albedo in North Pole and also of one half of IR flux over the complete orbit (see Figure 4-3 top right)

Including all contributors, the absorbed flux is varying of a factor x4 over the orbit. This large variation compared to the quasi constant hypothesis considered for the early predictions is the main contributor responsible for the mirror deformation over the orbit and its contribution to potential wind systematic errors. Indeed, the thermal control H/W (heaters and thermistors) implemented on the basis of the early predictions is now proven not adequate to control the actual perturbations seen by the mirror in orbit.

In addition to the environment contribution by itself, the selected thermal control law used for all thermal lines of the M1 in particular was not suitable to filter the gradients generated inside the M1 due to these environmental variations: in particular the single input single output (SISO) controller used prevents from getting a more efficient gradient compensation (a MIMO controller should have been used for some lines).

Despite these design limitations, in orbit tests have been run in 2020–2021 to tentatively optimize as much as possible the thermal control in order to decrease the gradients and their detrimental effects on the performances.

These tentative were first simulated with M1 thermal model and heating line control simulators. This allowed to find a new set of heating line coefficients.

The M1 thermal control updated parameters (heating line coefficients) have been confirmed through the thermal model. A preliminary set of parameter have been uploaded for test (6 & 7 July 2020): the results have shown that the M1 mean temperature variations was better correlated but not the radial gradients which was also confirmed as there was no wind speed bias improvement. This first in-flight thermal sensitivity tests allowed to validate the robustness of the wind speed bias correction algorithm developed by ECMWF.

A more complete set of parameters have been defined and are ready for an ultimate in-flight telescope thermal testing which is planned before AEOLUS satellite end of life deorbiting. This would complete the attempts to further improve the correlation made on ALADIN and allow collecting interesting lessons learnt for ALADIN Follow-on missions.

5. LESSONS LEARNT AND PERSPECTIVES

After a long and complex development period, AEOLUS mission is overpassing its demonstrator initial goals and the users (scientists community) have celebrated the third year in orbit with enthusiasm about the usefulness of the obtained data products results and the perspective of a follow on mission that would become operational over a wider time span.

While Aeolus follow on mission studies are ongoing, AEOLUS in orbit monitoring data analysis are still ongoing, and the processing outcome is not complete yet.

From the Airbus follow up of in orbit performance, several lessons learnt could be drawn:

- Long term energy evolution/stability is key for wind measurements performances: even if wind data measurement are still useful at lower level, the associated random error is increasing with signal decrease. The signal decrease root cause analysis is supported by the elaboration of the monitorings described in this paper: the main possible- but not definitively proven- root cause for this decay is considered linked to laser induced contamination or damage (even if not definitely proven) and to beam clipping. Lessons learnt on segregation of high fluence optics, larger field stop, realignment mechanism are thus taken into account for the next mission.
- Hot pixels: the Aeolus 2 detector study ongoing is tackling this observation with several workaround on operating temperature, on readout sequence optimization, material selection, and on improved near real time calibration operations.
- Thermal stability: the thermo-elastic stability improvement are essential to improve wind measurement bias and gain on wind data impact. The receiver bench was proven to be stable but the telescope and its thermal control will benefit from ALADIN lessons learnt as well as from the last 10 years of experience collected by Airbus on imagers for decreasing the impacts of orbital instabilities. In addition to telescope, the work on the receiver, with additional beam divergence sensor or with improved spectrometers, can largely compensate if not remove completely the M1 stability issues.
- Monitoring tools: the present paper describes all the available tools to follow the trend and monitor performance evolution. The experience gained on the available tools with their advantages and their limitations will guide the follow on instrument; energy, beam position and size and overall thermal maps appears keys for a better monitoring of performances allowing more precise and adequate corrections.
- Airbus ALADIN team participation to the in orbit performance follow up is considered as a good asset to support user team analysis and ensure best LIDAR end user data quality. Excellent collaboration have been achieved with AEOLUS DISC team (Data Innovation and Science Cluster), with DLR and with Leonardo team for laser operations.

REFERENCES

- [1] https://www.esa.int/Applications/Observing_the_Earth/FutureEO/Aeolus/Aeolus_laser_shines_light_on_wind
https://www.esa.int/Applications/Observing_the_Earth/FutureEO/Aeolus/Aeolus_wows_with_first_wind_data
https://www.esa.int/Applications/Observing_the_Earth/FutureEO/Aeolus/Aeolus_winds_now_in_daily_weather_forecasts
- [2] <https://amt.copernicus.org/articles/13/6007/2020/amt-13-6007-2020.html>
- [3] <https://amt.copernicus.org/articles/15/1465/2022/>
- [4] <https://amt.copernicus.org/articles/14/5153/2021/amt-14-5153-2021.html>
- [5] <https://amt.copernicus.org/articles/14/7167/2021/amt-14-7167-2021.html>